Hybridized Propagation of Spin Waves and Surface Acoustic Waves in a Multiferroic-Ferromagnetic Heterostructure

Jilei Chen,[1,2,3,§] Kei Yamamoto,[4,5,§] Jianyu Zhang,[2,§] Ji Ma,[6,§] Hanchen Wang,[1,2] Yuanwei Sun,[7] Mingfeng Chen,[6] Jing Ma,[6] Song Liu,[1,3] Peng Gao,[7] Dapeng Yu,[1,3] Jean-Philippe Ansermet,[3,8] Ce-Wen Nan,[6,*] Sadamichi Maekawa,[5,9,†] and Haiming Yu[1,2,‡]

[1]*International Quantum Academy, Shenzhen 518048, China*

[2]*Fert Beijing Institute, MIIT Key Laboratory of Spintronics, School of Integrated Circuit Science and Engineering, Beihang University, Beijing 100191, China*

[3]*Shenzhen Institute for Quantum Science and Engineering, Southern University of Science and Technology, Shenzhen, China*

[4]*Advanced Science Research Center, Japan Atomic Energy Agency, Tokai, Ibaraki 319-1195, Japan*

[5]*RIKEN Center for Emergent Matter Science, Wako, Saitama, Japan*

[6]*State Key Laboratory of New Ceramics and Fine Processing, School of Materials Science and Engineering, Tsinghua University, Beijing, China*

[7]*Interdisciplinary Institute of Light-Element Quantum Materials and Research Center for Light-Element Advanced Materials and International Center for Quantum Materials and Electron Microscopy Laboratory, School of Physics, Peking University, Beijing, China*

[8]*Institute of Physics, École Polytechnique Fédérale de Lausanne (EPFL), Lausanne, Switzerland*

[9]*Kavli Institute for Theoretical Sciences, University of Chinese Academy of Sciences, Beijing, China*

Coherent coupling in magnon-based hybrid systems has many potential applications in quantum information processing. Magnons can propagate in magnetically ordered materials without any motion of electrons, offering a unique method to build low-power-consumption devices and information channels free of heat dissipation. In this paper, we demonstrate the coherent propagation of hybridized modes between spin waves and Love surface acoustic waves in a multiferroic $BiFeO_3$ and ferromagnetic $La_{0.67}Sr_{0.33}MnO_3$-based heterostructure. The magnetoelastic coupling enables a giant enhancement of the strength of the hybridized mode by a factor of 26 compared to that of the pure spin waves. A short wavelength down to 250 nm is demonstrated for the hybridized mode, which is desirable for nanoscale acoustomagnonic applications. Our combined experimental and theoretical analyses represent a step towards the coherent control in hybrid magnonics, which may inspire the study of magnon-phonon hybrid systems for coherent information processing and manipulation.

I. INTRODUCTION

Coherent coupling between fundamental excitation attracts tremendous interests for information processing and quantum manipulations [1–6]. Quantum information can be conveyed from one platform to another through different media excitations, such as photons, phonons, and magnons. Magnons, as quanta of spin waves, are collective spin excitations in magnetic materials [7–14]. Spin

waves are considered as potential candidate for the next generation of information carriers beyond CMOS technology for low-power-consumption computing architectures because they can occur with no charge transport [15–20]. Spin waves, with a typical frequency range from GHz to THz and wavelengths from micrometer to nanometer, are promising for designing faster and smaller devices beyond the conventional computing paradigm. Hybrid magnonic quantum systems [21–24] enable coherent magnon interactions with microwave and optical photons [25–28], phonons [29–34], between superconducting qubits [4,35], and magnons themselves [36–38], offering further opportunities to develop quantum technologies for information processing. Surface acoustic waves (SAWs) are mechanically excited phonons, which have been widely used as sensors and resonators [39]. Full quantum control is also

---

*cwnan@mail.tsinghua.edu.cn

†sadamichi.maekawa@riken.jp

‡haiming.yu@buaa.edu.cn

§These authors contributed equally to this work.

demonstrated based on SAWs [40], harnessing various phononic devices [41–43].

Recently, the coherent coupling between spin waves and SAWs has seen a surge of interest [44–48]. The theoretical study of the parametric excitation of magnetic and elastic plane waves has a rich history exhibiting the methods of generation, amplification, and conversion of elastic and electromagnetic waves [49]. Elastically driven ferromagnetic resonance has been studied in lithium-niobate- ($LiNbO_3$) based devices such as $Ni/LiNbO_3$ [44] and $Co_{20}Fe_{60}B_{20}/LiNbO_3$ [45] by exciting Rayleigh-type SAW, and the magnetoelastic coupling is most efficient when the angle between the wave vector and the magnetization is at $45°$. However, in this configuration, the spin-wave dispersion is flat in the dipolar energy-dominated regime and the spin-wave propagation is suppressed [50]. Love SAWs are in-plane polarized shear phonons [51] propagating transverse to the wave vector, which are different from the predominantly longitudinal surface acoustic waves, such as Rayleigh waves. The latter is observed in most studies of acoustic ferromagnetic resonance. Ferroelectric $BiFeO_3$ (BFO) is recently found to host GHz coherent shear phonons' propagation with an efficiency much higher than in any metals and semiconductors due to a giant shear strain [52]. Although the shear strain cannot directly correspond to Love waves, it may indicate the possibility of studying the hybridization between Love SAWs and spin waves in $BiFeO_3/La_{0.67}Sr_{0.33}MnO_3$ (BFO/LSMO) heterostructures. The magnetoelastic coupling between horizontal shear SAWs and spin waves was recently demonstrated [53–55] and in contrast to Rayleigh SAW, the coupling strength reaches a maximum at 0 and $90°$. However, the phase-coherent propagation of the hybridized mode between Love SAWs and spin waves has not been reported yet, which can be an essential building block for acoustomagnonic logic devices and circuits.

In this work, we experimentally demonstrate the coherent propagation of hybridized mode between spin waves and Love SAWs in a composite system of BFO/LSMO heterostructures with phase-resolved propagating spin-wave spectroscopy. The BFO/LSMO heterostructure has been widely investigated in terms of its magnetoelectric property [56–62]. Spin waves at microwave frequencies propagate in ferromagnetic LSMO thin film and are coupled with Love SAWs at the interface with a multiferroic BFO layer via a magnetoelastic hybridization. The phase-coherent hybridized modes are observed when the dispersions of spin waves and phonons cross with each other. The signal strength of the magnetic field-dependent hybridized mode is enhanced by a factor of 26 compared to the amplitude of the pure spin-wave mode at the same wavelength. The shortest wavelength of the magnon-SAW hybridized mode is experimentally observed as 250 nm at around 12 GHz. Microwave antenna are very inefficient in exciting short-wavelength spin waves and phonons [44,45]. Instead, by

taking advantage of the magnetoelastic effect, we successfully realize hybrid propagation with a wavelength down to 250 nm. Furthermore, as the magnetoelastic coupling follows a $\cos2\theta$ dependence, where θ is the angle between the magnetization direction and the x axis as shown in Fig. 1(a), the magnetoelastic coupling reaches its maximum in the Damon-Eshbach (DE) and backward volume (BV) geometries, which is more attractive than the magnetoelastic coupling provided by Rayleigh waves [55]. The observed hybridization of Love SAWs in BFO and spin waves in LSMO is accounted for by a theoretical model, which includes an interfacial magnetoelastic coupling.

II. RESULTS AND DISCUSSION

Figure 1(a) illustrates the principle of the experiment. The BFO/LSMO heterostructure is deposited on the $NdGaO_3$ (001) substrate by KrF excimer pulsed-laser deposition with the energy of $1.5 \, J \, cm^{-2}$, a repetition rate of 5 Hz, and a wavelength of 248 nm. 80-nm-thick LSMO is first deposited at $780 °C$ with an oxygen partial pressure of 25 Pa. 20-nm-thick BFO is then deposited on top of LSMO at $700 °C$ with an oxygen partial pressure of 20 Pa. The annealing procedure is at 2×10^4 Pa oxygen partial pressure for 20 min and then cooling down to room temperature. The high-angle annular dark field image of the BFO/LSMO heterostructure near the interface is shown in Fig. 1(b). The characterization of energy-dispersive x-ray spectroscopy from selective elements is shown in Fig. S1 within the Supplemental Material [63]. Two identical nano-CPWs are patterned on top of the bilayer structure, with the width of signal and ground line equal to 130 nm and the gap in-between of 640 nm. The scanning electron microscope image of the nano-CPW is shown in Fig. S2 within the Supplemental Material [63]. The center-to-center distance s between two nano-CPWs is 4 μm. The k vectors of the excited spin waves depend on the design of the antennas and can be obtained by a Fourier transformation of the spatial magnetic excitation field distribution, and three prominent peaks marked by k_1, k_2, and k_3 are observed. The wave vector is along the in-plane pseudocubic (110) direction of the BFO film in the experiment. The all-electrical spin-wave measurement is conducted with an in-plane external magnetic field. By connecting the microwave antenna via microwave probes to a vector network analyzer (VNA), a rf current can be injected into the antenna. In order to improve the signal-to-noise ratio and remove the background drift signals, we present ΔS_{12} [Figs. 1(d) and 1(e)], which is the difference in the imaginary part of the VNA transmission spectra S_{12} taken at successive magnetic fields [64], as a function of $\mu_0 H$ and f at $\theta = 0°$ and $90°$. In Fig. 1(d), the field-dependent mode marked by a yellow arrow is the k_1 spin-wave mode in ferromagnetic LSMO film directly excited by the nano-CPW
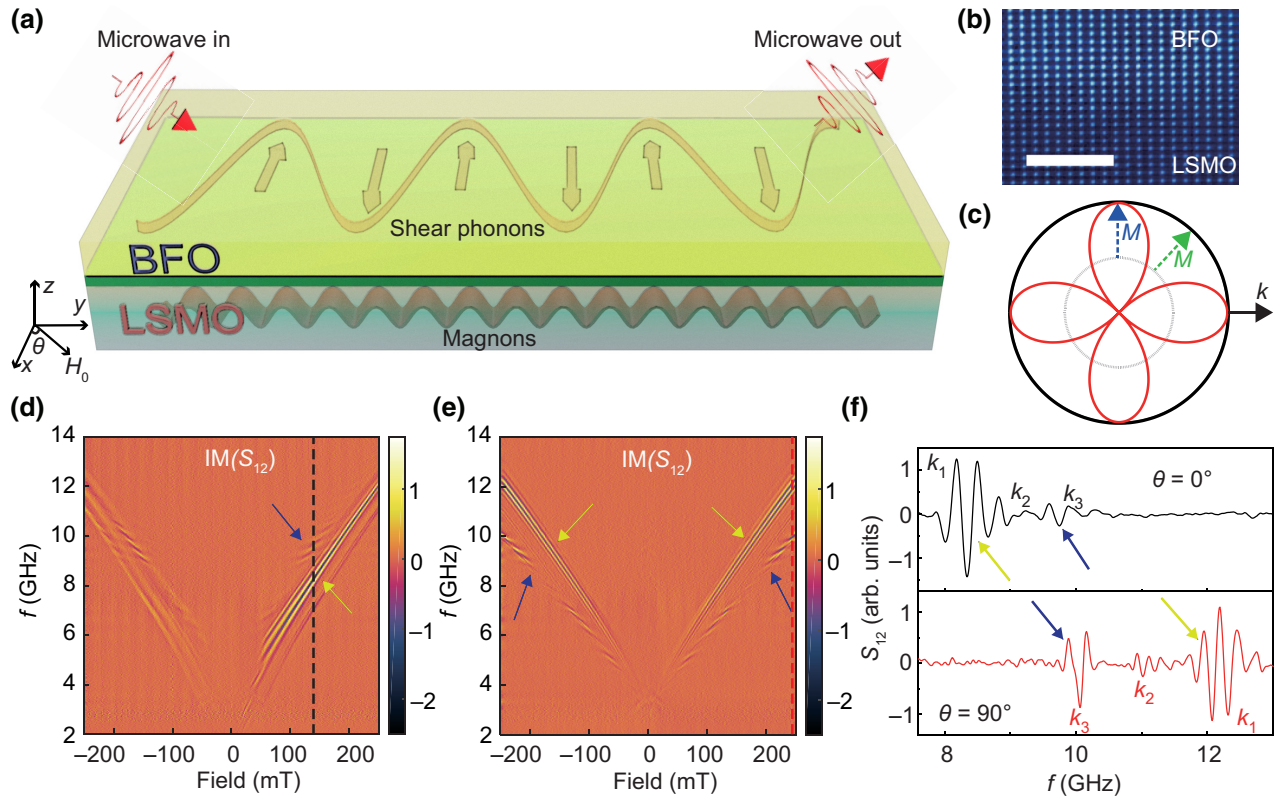
FIG. 1.　(a) Schematic of hybridized mode propagation in BFO/LSMO heterostructures. Microwaves are injected via nanoscale coplanar waveguides (CPWs) patterned on top of the sample. (b) Atomically resolved interface of BFO/LSMO by annular dark-field image. The scale bar is 2 nm. (c) Illustration of the isostrength contour of the magnetoelastic coupling between spin waves and Love SAWs. The blue arrow indicates the direction of the magnetization M and the black arrow shows the wave-vector direction. (d) The imaginary part of the spin-wave transmission spectra S_{12} at $\theta = 0°$, namely the DE configuration. Two distinct modes are marked in the figure by blue and yellow arrows. (e) The imaginary part of the spin-wave transmission spectra S_{12} at $\theta = 90°$, namely the BV configuration. (f) Single line cuts extracted from (d),(e) at 140 and 250 mT, respectively. Two separated modes are marked with blue and yellow arrows.

[Figs. 2(a) and 2(b)] [65]. The spectrum shows an asymmetry behavior at negative and positive fields due to the spin-wave nonreciprocity in the DE mode configuration [14]. Another mode beyond the k_1 spin-wave mode is observed and marked by blue arrows. Its phase oscillation extracted from the imaginary part of the transmission spectra shows a completely different behavior compared to the spin-wave mode. This mode is also found to be dependent on the field orientation and could be attributed to a mode hybridized between spin waves and another wave at higher wave vecotors than k_1. The perpendicular standing spin waves of the LSMO films resonate at frequencies > 13 GHz at around 200 mT and are not relevant for the additional mode marked by blue arrows[50]. Since BFO is a multiferroic material with a giant shear strain [52,66], this higher k wave corresponds to the acoustic waves. The strength of the hybridized mode reaches a maximum at $\theta = 0°$ and $90°$, which corresponds to the angular dependence of the magnetoelastic coupling between spin waves and Love SAWs [55] [Fig. 1(c)]. A theoretical model of the mode

hybridization is presented below, which quantitatively describes the hybridized propagation of spin waves and Love SAWs. When their dispersions cross, they hybridize with each other. At $\theta = 0°$, the DE mode frequency increases with the wave vector [50] and the frequency of the hybridization between spin waves and SAWs is higher than the k_1 spin-wave mode observed with the same antenna. Instead, in the BV configuration [Fig. 1(e)], the hybridized mode is below the k_1 spin-wave mode. The hybridized mode is also observed at around 10 GHz when acoustic-wave mode crosses with k_3 spin-wave mode. The spin-wave frequency decreases with increasing wave vector in the BV configuration [50], resulting in a lower frequency of the hybridized mode than k_1 spin-wave modes. Two linecuts extracted from the transmission spectra of Figs. 1(d) and 1(e) illustrate that the amplitude of the hybridized mode and the pure spin-wave mode are of the same order of magnitude. If the BFO layer is removed and the nano-CPWs are only patterned on the LSMO thin film, the hybridized mode vanishes, indicating that the BFO is
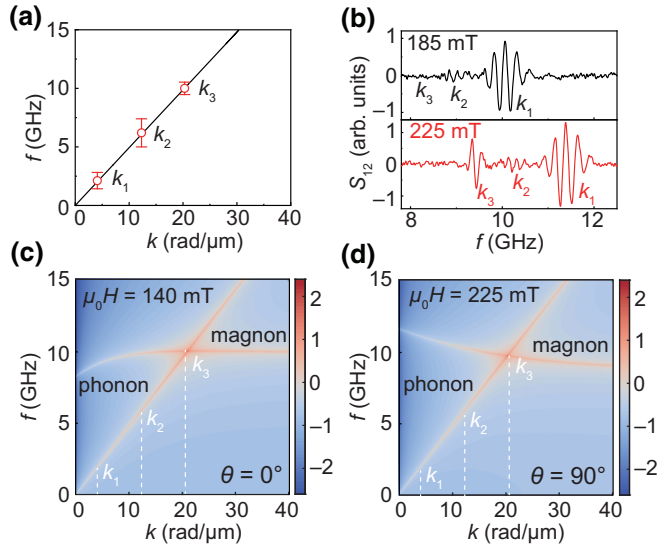
FIG. 2. (a) The SAW dispersion relation with the frequency extracted from the transmission spectra and the wave vector obtained from the Fourier transformation of nano-CPWs [see Fig. S2(c) within the Supplemental Material [63]]. (b) Linecuts extracted from the transmission spectra S_{12} at $\theta = 90°$, at 225 mT (with hybridized mode) and 185 mT (without hybridized mode), respectively. (c),(d) Theoretically calculated eigenfrequencies of the spin waves and SAWs as functions of the wave vector at $\theta = 0°$ and 90° at 140 and 225 mT, based on Eq. (1).

essential for the generation of the mode hybridization (see Fig. S3 within the Supplemental Material[63]).

Due to the discrete wave-vector distribution $k_1 = 4.1$ rad/µm, $k_2 = 12.2$ rad/µm, and $k_3 = 20.3$ rad/µm generated by the antenna, a linear fitting of the SAW dispersion could be performed, allowing us to extract the frequency of the magnon-SAW hybridized mode, as shown in Fig. 2(a). These three data points are extracted at the frequency of the hybridized modes at different magnetic fields in Fig. 1(d). The velocity of SAW from the linear dispersion yields a value of 3 km/s, which is much larger than that of spin waves in LSMO thin film [65]. In addition, the coherent hybridized mode excited by nano-CPWs exhibits finite wave-vector distribution, and the propagation over some distance accumulates a phase difference of $\Delta\phi = \Delta k \, s$, where s is the center-to-center distance between two nano-CPWs. Using the corresponding phase oscillation Δf, which indicates the phase accumulation of $\Delta\phi = 2\pi$, the group velocity could be estimated as [67]

$$v_g = \frac{\partial\omega}{\partial k} \approx \frac{2\pi\Delta f}{2\pi/s} = \Delta f \cdot s. \quad (1)$$

The group velocity of the hybridized mode at 10 GHz is calculated to be 1.2 km/s for DE configuration and 1.0 km/s for BV configuration, smaller than the velocity of pure SAWs due to the mode hybridization. At the

crossing point, the signal strength is found to be dramatically increased compared to k_3 spin-wave mode, shown in Fig. 2(b). Two linecuts at different magnetic fields are presented with (225 mT) and without (185 mT) the mode hybridization. The signal strength of k_3 spin-wave mode almost vanishes due to the low excitation efficiency of the nano-CPW. However, when the k_3 spin-wave mode hybridizes with Love SAWs, the signal strength is enhanced by a factor of 26. This large signal enhancement could be attributed to the field-independent SAW mode directly driven by the high-frequency electric field from the nano-CPWs, as presented in Fig. S4 within the Supplemental Material [63]. Note that the strength of hybridized mode is also larger than the CPW excited SAWs due to the mode hybridization. To further understand these experimental results, we investigate a theoretical model based on the interaction between spin waves and SAWs owing to a magnetoelastic coupling. We could observe from the experiment that at $\theta = 0°$ and 90°, the appearance of the magnon-SAW hybridized mode is completely different from the magnetoelastic coupling resulting from the longitudinal acoustic wave where the coupling vanishes at $\theta = 0°$ and 90°. The hybridization reflects the contribution of the Love SAWs. In this work, we consider the effective magnetoelastic coupling gives rise to the anticrossing behavior. The eigenfrequencies of the spin waves and Love SAWs are functions of the wave vector that can be expressed as [50,55]

$$\omega^2 = \frac{\left(c^2k^2 + \frac{\gamma^2 F_\parallel F_{zz}}{M_S^2}\right)}{2}$$
$$\pm \sqrt{\frac{\left(c^2k^2 - \frac{\gamma^2 F_\parallel F_{zz}}{M_S^2}\right)}{2} + \frac{4\gamma^2 F_{zz}|k|^3 d b_{\text{eff}}}{\rho M_S^2}\cos^2 2\theta}, \quad (2)$$

where c is the velocity of the SAW, γ is the gyromagnetic ratio, ρ is the mass density, M_S is the saturation magnetization of LSMO, d is the magnetic film thickness, $F_\parallel = \mu_0 M_S H_{\text{ext}} + \mu_0 M_S^2(1 - 1 - e^{-kd}/kd) + Ak^2 - K\cos2\theta$ and $F_{zz} = \mu_0 M_S H_{\text{ext}} + \mu_0 M_S^2 1 - e^{-kd}/kd + Ak^2 - K\sin^2\theta$ with A as the exchange constant and K as the uniaxial magnetic anisotropy. b_{eff} is set as 2×10^5 J/m^3 for the effective magnetoelastic coupling. The theoretically calculated transmission spectra mostly reproduce the experimental results [Figs. 1(d) and 1(e)] including both the pure spin-wave mode and the hybridized mode between spin waves and Love SAWs, as shown in Fig. S6 within the Supplemental Material [63]. The magnetoelastic coupling is maximized at $\theta = 90°$ and 0°, owing to the $\cos2\theta$ dependence, which is illustrated in Fig. 1(c). The thin-film approximation is applied with the ferromagnetic film whose thickness is much less than the wavelength
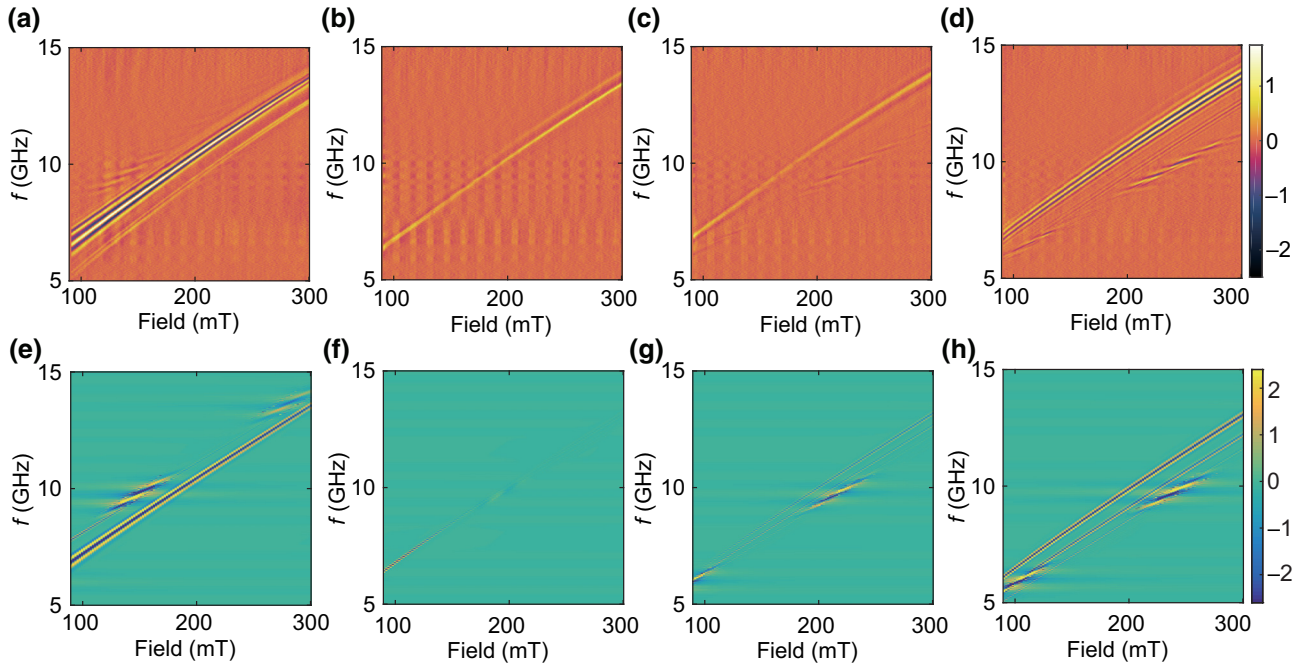
FIG. 3. (a)–(d) Experimentally obtained transmission spectra with $\theta = 0°$, $45°$, $60°$, and $90°$, respectively. The in-plane magnetic field is rotated with respect to the wave vector. The external magnetic field is swept from 90 to 300 mT with the step of 1 mT. (e)–(h) Theoretically calculated transmission spectra with $\theta = 0°$, $45°$, $60°$, and $90°$.

and also much less than the thickness of the elastic body, where the SAW is considered localized. The detailed theoretical calculations can be found in Fig. S7 within the Supplemental Material [63].

The calculated eigenfrequencies of spin waves and SAWs as a function of the wave vector are shown in Figs. 2(c) and 2(d) for DE and BV configuration, respectively. In Fig. 2(c), the external magnetic field is fixed at 150 mT and one could observe that the crossing between the spin-wave branch and acoustic-wave branch is at around 10 GHz. The dispersion of BV mode spin waves possesses a negative slope in the dipolar regime, and the frequency of the spin-wave mode with smaller wave vector is higher than the crossing point. The anticrossing behavior between two coupled modes is not prominent due to the weak magnetoelastic coupling. Detailed calculation based on different coupling strength is shown below.

The angular-dependent measurements are presented in Fig. 3. According to Eq. (1), the magnetoelastic coupling between spin waves and Love waves follows a $\cos 2\theta$ dependence. Figures 3(a)–3(d) show the experimental transmission spectra from $\theta = 0°$ and $90°$. One can observe that when the angle deviates from $0°$ to $90°$, the signal strength of the hybridized mode becomes weaker. At $45°$, the coherent hybridized mode vanishes, indicating the absence of magnetoelastic coupling. The angular-dependent behavior of magnetoelastic coupling is completely different from the coupling that originated from longitudinal SAWs, which have been commonly

observed in LiNbO$_3$-based hybrid systems [44]. At $45°$, the spin-wave dispersion is flat compared to $0°$ or $90°$, implying that spin waves have a very small group velocity and the propagation is suppressed. The angular dependence found in our experiments is therefore attractive for alternative applications based on coherent magnon-SAW hybridized waves considering the optimized propagating properties in contrast to the Rayleigh-wave-based hybridization. One could observe a prominent magnetic-field-dependent mode at $45°$, which could be attributed to the incoherent magnon-phonon mode without the phase oscillation, and has been discussed in Ref. [48]. The other
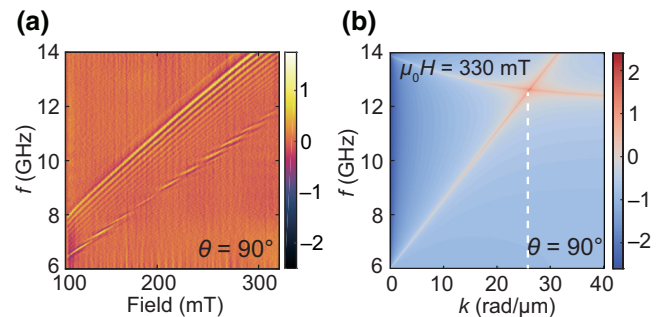

FIG. 4. (a) The transmission spectra S_{12} at $\theta = 90°$ measured by NSL antenna. (b) Theoretically calculated eigenfrequencies of the spin waves and SAWs as functions of the wave vector at $\theta = 90°$ at 330 mT based on Eq. (1). The white dashed line indicates the highest wave vector observed in the experiment.
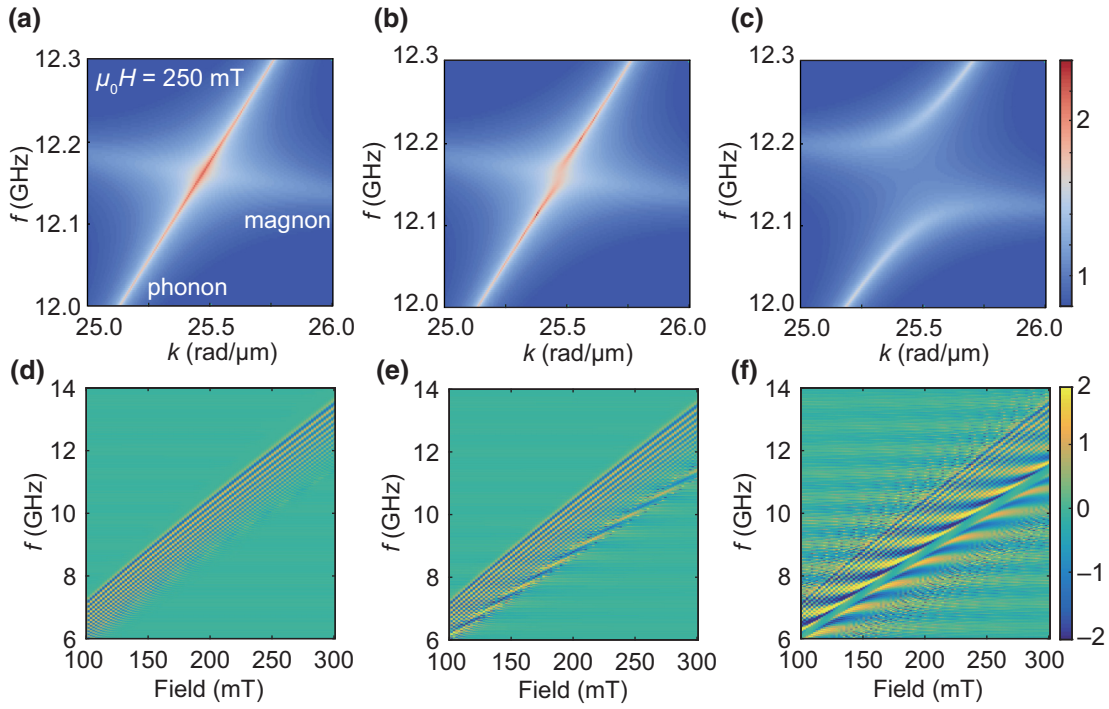
FIG. 5. (a)–(c) Enlarged images of the theoretically calculated eigenfrequencies of the spin waves and SAWs as functions of the wave vector at $\theta = 90°$ at 250 mT, with $b_{\mathrm{eff}} = 2 \times 10^4$ J/m^3, 2×10^5 J/m^3, and 1×10^6 J/m^3, respectively. (d)–(f) Calculated transmission spectra at $\theta = 90°$, corresponding to the (a)–(c).

angular-dependent measurements with different angles can be found in Fig. S8 within the Supplemental Material [63]. The theoretical calculations in Figs. 3(e)–3(h) reproduce well the angular dependence of the hybridized mode in the experiment and the hybridized modes are prominent at $\theta = 0°$ and $90°$. One could also observe the reduction of the pure propagating spin-wave signal in the spectra at 45° due to the flatness of the spin-wave dispersion [50].

In the following, we replace the nano-CPW antenna by the nanostripline (NSL), which provides the excitation over a broadband wave-vector range (see Fig. S9 within the Supplemental Material for the Fourier transformation of NSL [63]) . The width of the NSL is 100 nm and the separation distance between two NSLs is fixed at 4 μm. Figure 4(a) shows the measured transmission spectra with $\theta = 90°$. An apparent broadband excitation of propagating spin-wave mode is observed, without discrete modes depending on the wave-vector distribution of NSLs. The magnon-SAW hybridized mode is also observed to exist in all frequency bands. The theoretically calculated spectra corresponding to Fig. 4(a) is shown in Fig. 5(e). With increasing the external magnetic field, the frequency of spin-wave mode also increases following [50]:

$$\omega^2_{\mathrm{MSBVW}} = \omega_H \left[\omega_H + \omega_M \left(\frac{1 - e^{-kd}}{kd} \right) \right], \quad (3)$$

with $\omega_M = \gamma \mu_0 M_S$ and $\omega_H = \gamma \mu_0 H_{\mathrm{ext}}$. The frequency of the crossing point between spin waves and SAWs also increases with respect to the external magnetic field. In the experiment, when the external magnetic field is fixed at 330 mT, the magnon-SAW hybridization appears at 12 GHz, corresponding to a wave vector of 25.6 rad/μm and a wavelength of 250 nm as shown in Fig. 4(b). Here, the magnetoelastic coupling is not in the strong coupling regime, therefore, the anticrossing behavior is not obvious. The wavelength of the observed short-wavelength magnon-SAW coupled waves is much smaller than that from the LiNbO$_3$-based systems with the microwave antenna of interdigital transducers (IDT) [44,45]. In addition, the wave vector here is beyond the resolution limit of Brillouin light scattering (BLS) systems, a technique widely used for studying spin waves [68].

Finally, the effective magnetoelastic coupling strength b_{eff} for tuning the magnon-SAW hybridized mode is investigated in Fig. 5. The theoretical analysis is based on the NSL antenna with a broadband wave-vector distribution. When the effective coupling $b_{\mathrm{eff}} = 2 \times 10^4$ J/m^3 is weak as shown in Fig. 5(a), one could observe that the anticrossing behavior at the crossing point is not prominent, and the two modes are not effectively coupled. The calculated transmission spectra also show the absence of the magnon-SAW hybridized mode [Fig. 5(d)]. However, if the effective magnetoelastic coupling strength b_{eff} is increased to 2×10^5 J/m^3, although the anticrossing is still not evident

due to the relatively high dissipation rate of the magnon, the spin wave and the acoustic-wave modes settled as distorted at the crossing point. Here, the Gilbert damping of LSMO is set as 1.2×10^{-3} [48]. The system is in the weak-coupling regime nevertheless the mode hybridization is evident in transmission, as shown in Fig. 5(e). The theoretical calculation results with $b_{\text{eff}} = 2 \times 10^5$ J/m³ are very close to the experimental observation [Fig. 4(a)]. Furthermore, when the effective magnetoelastic coupling strength b_{eff} is increased to the value of 1×10^6 J/m³, the anticrossing between two coupled modes is very distinct and the system is in the strong coupling regime. The anticrossing gap also arises in the calculated transmission spectra, while such highly effective magnetoelastic coupling is unable to correspond to the experimental results. Note that we consider the effective magnetoelastic coupling shows an anticrossing behavior. Recently, the level attraction originated from the dissipative coupling exhibited in a magnon-photon hybridized system [69]. If instead, we consider the coupling type of level attraction, the phase oscillation behavior is different from the experimental results, as shown in Fig. S10 within the Supplemental Material [63].

III. CONCLUSION

In conclusion, we experimentally observe the coherent propagation of the hybridization mode between spin waves and Love waves in a multiferroic-ferromagnetic heterostructure composed of BFO and LSMO, respectively. The hybridization appears when the dispersions of spin waves and Love SAWs cross with one another. In contrast to the typical magnon-phonon coupling involving the Rayleigh waves, the hybridization with Love waves follows a cos2θ dependence, thus presenting a maximum strength in DE and BV configurations. Furthermore, the hybridized mode exhibits much larger intensity than the spin-wave mode directly excited by CPWs. The shortest wavelength of 250 nm is observed when mode hybridization takes place. A mode of such a small wavelength would be very difficult to excite with our antennas if the BFO layer and its Love mode were not coupled to the spin-wave modes in LSMO. This enhancement is a critical feature that paves the way for nanoscale-integrated magnetoacoustic devices.

ACKNOWLEDGMENTS

[1] A. Frisk Kockum, A. Miranowicz, S. De Liberato, S. Savasta, and F. Nori, Ultrastrong coupling between light and matter, Nat. Rev. Phys. **1**, 19 (2019).

[2] X. Zhu, S. Saito, A. Kemp, K. Kakuyanagi, S.-i. Karimoto, H. Nakano, W. J. Munro, Y. Tokura, M. S. Everitt, and K. Nemoto, *et al.*, Coherent coupling of a superconducting flux qubit to an electron spin ensemble in diamond, Nature **478**, 221 (2011).

[3] E. Verhagen, S. Deléglise, S. Weis, A. Schliesser, and T. J. Kippenberg, Quantum-coherent coupling of a mechanical oscillator to an optical cavity mode, Nature **482**, 63 (2012).

[4] Y. Tabuchi, S. Ishino, A. Noguchi, T. Ishikawa, R. Yamazaki, K. Usami, and Y. Nakamura, Coherent coupling between a ferromagnetic magnon and a superconducting qubit, Science **349**, 405 (2015).

[5] L. Zhang, F. Wu, S. Hou, Z. Zhang, Y.-H. Chou, K. Watanabe, T. Taniguchi, S. R. Forrest, and H. Deng, Van der Waals heterostructure polaritons with moiré-induced nonlinearity, Nature **591**, 61 (2021).

[6] J. Majer, J. Chow, J. Gambetta, J. Koch, B. Johnson, J. Schreier, L. Frunzio, D. Schuster, A. A. Houck, and A. Wallraff, *et al.*, Coupling superconducting qubits via a cavity bus, Nature **449**, 443 (2007).

[7] A. Barman, G. Gubbiotti, S. Ladak, A. O. Adeyeye, M. Krawczyk, J. Gräfe, C. Adelmann, S. Cotofana, A. Naeemi, and V. I. Vasyuchka, *et al.*, The 2021 magnonics roadmap, J. Phys. Condens. Matter **33**, 413001 (2021).

[8] P. Pirro, V. I. Vasyuchka, A. A. Serga, and B. Hillebrands, Advances in coherent magnonics, Nat. Rev. Mater. **6**, 1114 (2021).

[9] A. V. Chumak, V. I. Vasyuchka, A. A. Serga, and B. Hillebrands, Magnon spintronics, Nat. Phys. **11**, 453 (2015).

[10] D. Grundler, Nanomagnonics around the corner, Nat. Nanotechnol. **11**, 407 (2016).

[11] V. Kruglyak, S. Demokritov, and D. Grundler, Magnonics, J. Phys. D: Appl. Phys **43**, 264001 (2010).

[12] B. Lenk, H. Ulrichs, F. Garbs, and M. Münzenberg, The building blocks of magnonics, Phys. Rep. **507**, 107 (2011).

[13] H. Yu, J. Xiao, and H. Schultheiss, Magnetic texture based magnonics, Phys. Rep. **905**, 1 (2021).

[14] J. Chen, H. Yu, and G. Gubbiotti, Unidirectional spin-wave propagation and devices, J. Phys. D: Appl. Phys. **55**, 123001 (2021).

[15] B. Dieny, I. L. Prejbeanu, K. Garello, P. Gambardella, P. Freitas, R. Lehndorff, W. Raberg, U. Ebels, S. O. Demokritov, and J. Akerman, *et al.*, Opportunities and challenges for spintronics in the microelectronics industry, Nat. Electron. 3, 446 (2020).

[16] J. Lan, W. Yu, R. Wu, and J. Xiao, Spin-Wave Diode, Phys. Rev. X 5, 041049 (2015).

[17] A. V. Chumak, A. A. Serga, and B. Hillebrands, Magnon transistor for all-magnon data processing, Nat. Commun. 5, 4700 (2014).

[18] Q. Wang, M. Kewenig, M. Schneider, R. Verba, F. Kohl, B. Heinz, M. Geilen, M. Mohseni, B. Lägel, and F. Ciubotaru, *et al.*, A magnonic directional coupler for integrated magnonic half-adders, Nat. Electron. 3, 765 (2020).

[19] J. Chen, H. Wang, T. Hula, C. Liu, S. Liu, T. Liu, H. Jia, Q. Song, C. Guo, and Y. Zhang, *et al.*, Reconfigurable spin-wave interferometer at the nanoscale, Nano Lett. 21, 6237 (2021).

[20] R. Li, P. Li, D. Yi, L. J. Riddiford, Y. Chai, Y. Suzuki, D. C. Ralph, and T. Nan, Anisotropic magnon spin transport in ultrathin spinel ferrite thin films-evidence for anisotropy in exchange stiffness, Nano Lett. 22, 1167 (2022).

[21] H. Yuan, Y. Cao, A. Kamra, R. A. Duine, and P. Yan, Quantum magnonics: When magnon spintronics meets quantum information science, Phys. Rep. 965, 1 (2022).

[22] D. D. Awschalom, C. R. Du, R. He, F. J. Heremans, A. Hoffmann, J. Hou, H. Kurebayashi, Y. Li, L. Liu, and V. Novosad, *et al.*, Quantum engineering with hybrid magnonic systems and materials, IEEE Trans. Quantum Eng. 2, 1 (2021).

[23] Y. Li, W. Zhang, V. Tyberkevych, W.-K. Kwok, A. Hoffmann, and V. Novosad, Hybrid magnonics: Physics, circuits, and applications for coherent information processing, J. Appl. Phys. 128, 130902 (2020).

[24] I. A. Golovchanskiy, N. N. Abramov, V. S. Stolyarov, P. S. Dzhumaev, O. V. Emelyanova, A. A. Golubov, V. V. Ryazanov, and A. V. Ustinov, Ferromagnet/superconductor hybrid magnonic metamaterials, Adv. Sci. 6, 1900435 (2019).

[25] H. Huebl, C. W. Zollitsch, J. Lotze, F. Hocke, M. Greifenstein, A. Marx, R. Gross, and S. T. B. Goennenwein, High Cooperativity in Coupled Microwave Resonator Ferrimagnetic Insulator Hybrids, Phys. Rev. Lett. 111, 127003 (2013).

[26] X. Zhang, C.-L. Zou, L. Jiang, and H. X. Tang, Strongly Coupled Magnons and Cavity Microwave Photons, Phys. Rev. Lett. 113, 156401 (2014).

[27] L. Bai, M. Harder, Y. P. Chen, X. Fan, J. Q. Xiao, and C.-M. Hu, Spin Pumping in Electrodynamically Coupled Magnon-Photon Systems, Phys. Rev. Lett. 114, 227201 (2015).

[28] J. Xu, C. Zhong, X. Han, D. Jin, L. Jiang, and X. Zhang, Coherent Gate Operations in Hybrid Magnonics, Phys. Rev. Lett. 126, 207202 (2021).

[29] J. Holanda, D. Maior, A. Azevedo, and S. Rezende, Detecting the phonon spin in magnon–phonon conversion experiments, Nat. Phys. 14, 500 (2018).

[30] K. An, R. Kohno, A. N. Litvinenko, R. L. Seeger, V. V. Naletov, L. Vila, G. de Loubens, J. BenYoussef, N. Vukadinovic, and G. E. W. Bauer, *et al.*, Bright and Dark States of two Distant Macrospins Strongly Coupled by Phonons, Phys. Rev. X 12, 011060 (2022).

[31] Y. Kurimune, M. Matsuo, and Y. Nozaki, Observation of Gyromagnetic Spin Wave Resonance in NiFe Films, Phys. Rev. Lett. 124, 217205 (2020).

[32] A. Rückriegel and R. A. Duine, Long-Range Phonon Spin Transport in Ferromagnet–Nonmagnetic Insulator Heterostructures, Phys. Rev. Lett. 124, 117201 (2020).

[33] C. Berk, M. Jaris, W. Yang, S. Dhuey, S. Cabrini, and H. Schmidt, Strongly coupled magnon–phonon dynamics in a single nanomagnet, Nat. Commun. 10, 2652 (2019).

[34] X. Zhang, C.-L. Zou, L. Jiang, and H. X. Tang, Cavity magnomechanics, Sci. Adv. 2, e1501286 (2016).

[35] D. Lachance-Quirion, S. P. Wolski, Y. Tabuchi, S. Kono, K. Usami, and Y. Nakamura, Entanglement-based single-shot detection of a single magnon with a superconducting qubit, Science 367, 425 (2020).

[36] D. MacNeill, J. T. Hou, D. R. Klein, P. Zhang, P. Jarillo-Herrero, and L. Liu, Gigahertz Frequency Antiferromagnetic Resonance and Strong Magnon-Magnon Coupling in the Layered Crystal CrCl$_3$, Phys. Rev. Lett. 123, 047204 (2019).

[37] Y. Li, W. Cao, V. P. Amin, Z. Zhang, J. Gibbons, J. Sklenar, J. Pearson, P. M. Haney, M. D. Stiles, and W. E. Bailey, *et al.*, Coherent Spin Pumping in a Strongly Coupled Magnon-Magnon Hybrid System, Phys. Rev. Lett. 124, 117202 (2020).

[38] J. Chen, C. Liu, T. Liu, Y. Xiao, K. Xia, G. E. W. Bauer, M. Wu, and H. Yu, Strong Interlayer Magnon-Magnon Coupling in Magnetic Metal-Insulator Hybrid Nanostructures, Phys. Rev. Lett. 120, 217202 (2018).

[39] P. Delsing, A. N. Cleland, M. J. Schuetz, J. Knörzer, G. Giedke, J. I. Cirac, K. Srinivasan, M. Wu, K. C. Balram, and C. Bäuerle, *et al.*, The 2019 surface acoustic waves roadmap, J. Phys. D: Appl. Phys. 52, 353001 (2019).

[40] K. J. Satzinger, Y. Zhong, H.-S. Chang, G. A. Peairs, A. Bienfait, M.-H. Chou, A. Cleland, C. R. Conner, É. Dumur, and J. Grebel, *et al.*, Quantum control of surface acoustic-wave phonons, Nature 563, 661 (2018).

[41] H. He, C. Qiu, L. Ye, X. Cai, X. Fan, M. Ke, F. Zhang, and Z. Liu, Topological negative refraction of surface acoustic waves in a Weyl phononic crystal, Nature 560, 61 (2018).

[42] K. Y. Bliokh and F. Nori, Klein-Gordon Representation of Acoustic Waves and Topological Origin of Surface Acoustic Modes, Phys. Rev. Lett. 123, 054301 (2019).

[43] L. Shao, W. Mao, S. Maity, N. Sinclair, Y. Hu, L. Yang, and M. Lončar, Non-reciprocal transmission of microwave acoustic waves in nonlinear parity–time symmetric resonators, Nat. Electron. 3, 267 (2020).

[44] M. Weiler, L. Dreher, C. Heeg, H. Huebl, R. Gross, M. S. Brandt, and S. T. B. Göennenwein, Elastically Driven Ferromagnetic Resonance in Nickel Thin Films, Phys. Rev. Lett. 106, 117601 (2011).

[45] M. Xu, K. Yamamoto, J. Puebla, K. Baumgaertl, B. Rana, K. Miura, H. Takahashi, D. Grundler, S. Maekawa, and Y. Otani, Nonreciprocal surface acoustic wave propagation via magneto-rotation coupling, Sci. Adv. 6, eabb1724 (2020).

[46] M. Küß, M. Heigl, L. Flacke, A. Hörner, M. Weiler, M. Albrecht, and A. Wixforth, Nonreciprocal Dzyaloshinskii-Moriya Magnetoacoustic Waves, Phys. Rev. Lett. **125,** 217203 (2020).

[47] C. Zhao, Y. Li, Z. Zhang, M. Vogel, J. E. Pearson, J. Wang, W. Zhang, V. Novosad, Q. Liu, and A. Hoffmann, Phonon Transport Controlled by Ferromagnetic Resonance, Phys. Rev. Appl. **13,** 054032 (2020).

[48] J. Zhang, M. Chen, J. Chen, K. Yamamoto, H. Wang, M. Hamdi, Y. Sun, K. Wagner, W. He, and Y. Zhang, *et al.*, Long decay length of magnon-polarons in $BiFeO_3/La_{0.67}Sr_{0.33}MnO_3$ heterostructures, Nat. Commun. **12,** 7258 (2021).

[49] R. Comstock, Parametric coupling of the magnetization and strain in a ferrimagnet. II. Parametric excitation of magnetic and elastic plane waves, J. Appl. Phys. **34,** 1465 (1963).

[50] B. Kalinikos and A. Slavin, Theory of dipole-exchange spin wave spectrum for ferromagnetic films with mixed exchange boundary conditions, J. Phys. C Solid State Phys. **19,** 7013 (1986).

[51] T. Funato and M. Matsuo, Helicity current generation by distorted Rashba coupling, Phys. Rev. B **104,** L060412 (2021).

[52] M. Lejman, G. Vaudel, I. C. Infante, P. Gemeiner, V. E. Gusev, B. Dkhil, and P. Ruello, Giant ultrafast photo-induced shear strain in ferroelectric $BiFeO_3$, Nat. Commun. **5,** 4301 (2014).

[53] N. K. Babu, A. Trzaskowska, P. Graczyk, G. Centała, S. Mieszczak, H. Głowinski, M. Zdunek, S. Mielcarek, and J. W. Kłos, The interaction between surface acoustic waves and spin waves: The role of anisotropy and spatial profiles of the modes, Nano Lett. **21,** 946 (2020).

[54] M. Küß, M. Heigl, L. Flacke, A. Hefele, A. Hörner, M. Weiler, M. Albrecht, and A. Wixforth, Symmetry of the Magnetoelastic Interaction of Rayleigh and Shear Horizontal Magnetoacoustic Waves in Nickel Thin Films on $LiTaO_3$, Phys. Rev. Appl. **15,** 034046 (2021).

[55] K. Yamamoto, M. Xu, J. Puebla, Y. Otani, and S. Maekawa, Interaction between surface acoustic waves and spin waves in a ferromagnetic thin film, J. Magn. Magn. Mater. **545,** 168672 (2022).

[56] M. Fiebig, T. Lottermoser, D. Meier, and M. Trassin, The evolution of multiferroics, Nat. Rev. Mater. **1,** 16046 (2016).

[57] J. Ma, J. Hu, Z. Li, and C.-W. Nan, Recent progress in multiferroic magnetoelectric composites: From bulk to thin films, Adv. Mater. **23,** 1062 (2011).

[58] N. A. Spaldin and R. Ramesh, Advances in magnetoelectric multiferroics, Nat. Mater. **18,** 203 (2019).

[59] J. Wang, J. Neaton, H. Zheng, V. Nagarajan, S. Ogale, B. Liu, D. Viehland, V. Vaithyanathan, D. Schlom, and U. Waghmare, *et al.*, Epitaxial $BiFeO_3$ multiferroic thin film heterostructures, Science **299,** 1719 (2003).

[60] T. Choi, S. Lee, Y. Choi, V. Kiryukhin, and S.-W. Cheong, Switchable ferroelectric diode and photovoltaic effect in $BiFeO_3$, Science **324,** 63 (2009).

[61] D. Yi, P. Yu, Y.-C. Chen, H.-H. Lee, Q. He, Y.-H. Chu, and R. Ramesh, Tailoring magnetoelectric coupling in $BiFeO_3/La_{0.7}Sr_{0.3}MnO_3$ heterostructure through the interface engineering, Adv. Mater. **31,** 1806335 (2019).

[62] S. Singh, J. T. Haraldsen, J. Xiong, E. M. Choi, P. Lu, D. Yi, X.-D. Wen, J. Liu, H. Wang, and Z. Bi, *et al.*, Induced Magnetization in $La_{0.7}Sr_{0.3}MnO_3/BiFeO_3$ Superlattices, Phys. Rev. Lett. **113,** 047204 (2014).

[63] See Supplemental Material at http://link.aps.org/supplemental/10.1103/PhysRevApplied.19.024046 for energy dispersive x-ray spectroscopy, BFO/LSMO heterostructure sketch and nano-CPWs, measurement results of bare LSMO sample without BFO capping layer, field-independent SAW mode driven by nano-CPWs, theoretical model, angular dependent measurements, full transmission spectra with nanostripline antennae and theoretical results for the dissipative coupling.

[64] P. Che, K. Baumgaertl, A. Kúkolova, C. Dubs, and D. Grundler, Efficient wavelength conversion of exchange magnons below 100 nm by magnetic coplanar waveguides, Nat. Commun. **11,** 1445 (2020).

[65] J. Zhang, A. A. Burema, J. Chen, J. Hu, C. Guo, H. Wang, N. Li, B. Wei, X. Han, and T. Banerjee, *et al.*, Surface anisotropy induced spin wave nonreciprocity in epitaxial $La_{0.33}Sr_{0.67}MnO_3$ film on $SrTiO_3$ substrate, Appl. Phys. Lett. **117,** 232402 (2020).

[66] P. Ruello, T. Pezeril, S. Avanesyan, G. Vaudel, V. Gusev, I. C. Infante, and B. Dkhil, Photoexcitation of gigahertz longitudinal and shear acoustic waves in $BiFeO_3$ multiferroic single crystal, Appl. Phys. Lett. **100,** 212906 (2012).

[67] C. Liu, S. Wu, J. Zhang, J. Chen, J. Ding, J. Ma, Y. Zhang, Y. Sun, S. Tu, and H. Wang, *et al.*, Current-controlled propagation of spin waves in antiparallel, coupled domains, Nat. Nanotechnol. **14,** 691 (2019).

[68] M. Madami, S. Bonetti, G. Consolo, S. Tacchi, G. Carlotti, G. Gubbiotti, F. Mancoff, M. A. Yar, and J. Åkerman, Direct observation of a propagating spin wave induced by spin-transfer torque, Nat. Nanotechnol. **6,** 635 (2011).

[69] M. Harder, Y. Yang, B. M. Yao, C. H. Yu, J. W. Rao, Y. S. Gui, R. L. Stamps, and C.-M. Hu, Level Attraction Due to Dissipative Magnon-Photon Coupling, Phys. Rev. Lett. **121,** 137203 (2018).